*crystals*

*Article*

# Modulation Effect of Hardness on the Friction Coefficient and Its Mechanism Analysis of $ZrB_2$/Mo Multilayers Synthesized by Magnetron Sputtering

**Tingjia Zhang, Lei Dong *, Jie Wu and Dejun Li ***

College of Physics and Materials Science, Tianjin Normal University, Tianjin 300387, China; ztj960108@126.com (T.Z.); jiewu@tjnu.edu.cn (J.W.)
* Correspondence: dlei0008@tjnu.edu.cn (L.D.); dejunli@tjnu.edu.cn (D.L.); Tel.: +86-22-2376-6519 (D.L.)

**Abstract:** $ZrB_2$/Mo multilayers were prepared by the magnetron sputtering technique on Si (100) and $Al_2O_3$ (001) substrates. The friction behavior and wear mechanism of the multilayers were tested at variable modulation ratios ($t_{ZrB2}$:$t_{Mo}$) of 1:1 to 8:1 at different temperatures. Under the influence of an effective modulation ratio and temperature, the friction coefficient and hardness of $ZrB_2$/Mo multilayers showed an almost opposite change rule, that is, the higher the hardness, the lower the friction coefficient. The hardness and elastic modulus reached the maximum value (26.1 GPa and 241.99 GPa) at $t_{ZrB2}$:$t_{Mo}$ = 5:1 and the corresponding friction coefficient was 0.86. Meanwhile, the hardness and average friction coefficient at 500 °C were, respectively, 8.9 GPa and 1.23. First-principles calculations of the interface model of $ZrB_2$ (001)/Mo (110) showed that the ionic bonds and covalent bonds at the interface can effectively improve the viscosity of the multilayer and the stability of the interface, and thus increase the hardness. This also indicated that the variation of the friction coefficient was mainly determined by the stability of the interface in the $ZrB_2$/Mo multilayers.

**Keywords:** $ZrB_2$/Mo multilayers; modulation ratio; friction coefficient; first principles calculation; the stability of the interface

check for updates

**Citation:** Zhang, T.; Dong, L.; Wu, J.; Li, D. Modulation Effect of Hardness on the Friction Coefficient and Its Mechanism Analysis of $ZrB_2$/Mo Multilayers Synthesized by Magnetron Sputtering. *Crystals* **2021**, *11*, 69. https://doi.org/10.3390/cryst11010069

Received: 28 November 2020
Accepted: 15 January 2021
Published: 16 January 2021



## 1. Introduction

Over the past few decades, microelectronics and micromachining technologies have made remarkable achievements, but these are deeply dependent on the development and application of new nano-films and coatings. Microelectronic devices are used more and more in extreme environments such as high temperature and strong corrosive environments, which puts forward higher requirements on the synthesis technology and material properties of related coatings, especially on their mechanical properties and friction resistance properties [1,2].

Many surface modification techniques, including thermal spraying [3], laser cladding [4], and ion implantation [5], can improve the high temperature wear resistance of materials to a certain extent. However, they also have various shortcomings, such as excessive porosity of the membrane and complicated processing procedures, which largely limit their development and application in the field of micro-electromechanics. In contrast, magnetron sputtering technology can effectively control the composition and microstructure of the film by adjusting the sputtering parameters, thereby preparing a dense and uniform multilayer with strong adhesion, which can avoid the disadvantages of the above-mentioned synthesis technology.

At the same time, the composite coating material can improve the high temperature friction resistance of the film very well, but the formation mechanism of this material is very complicated, and the improvement result has great uncertainty. For example, by combining transition metal sulfides ($MoS_2$ or $WS_2$) and oxides (PbO or ZnO) to form $PbMoO_4$ or $ZnWO_4$, it can provide good lubrication at higher temperatures [6,7]; in $Mo_2N/MoS_2$/Ag systems, it was found that the friction coefficient of silver molybdate formed on the surface at high temperature is low [8,9]. However, the poor mechanical strength greatly affects the service life of these films.

Therefore, it is necessary to establish a method that can effectively improve the mechanical properties, high temperature resistance, and friction properties of the multilayer. Among many materials, $ZrB_2$ has the advantages of a high melting point, high hardness, low density, excellent corrosion resistance and oxidation resistance [10–16], and it is a promising ultra-high temperature ceramic material. Over the years, despite extensive research on the microstructure and mechanical properties of $ZrB_2$ [17,18], its application was still limited by its inherent brittleness, low fracture toughness, and unreliable high temperature performance [19,20]. The hardness of metallic molybdenum Mo (9.7 GPa) is lower than that of $ZrB_2$ (23 GPa), but its crystal structure can form a higher lattice-matching degree with $ZrB_2$. In addition, Mo's anti-friction and corrosion-resistance performance is better, and its friction coefficient (0.2) significantly lower than those of $ZrB_2$ (0.5), and it has higher high-temperature resistance.

In this work, we designed and prepared a series of $ZrB_2$/Mo multilayer systems with the same modulation period (25 nm) and different modulation ratios. The purpose was to establish and improve the high-temperature abrasion resistance by analyzing the regulation of its hardness. It is a simple method, and first-principles calculation reveals the mechanism of how hardness adjusts the high-temperature friction performance.

## 2. Experimental Details

$ZrB_2$/Mo multilayers along with $ZrB_2$ and Mo monolayers were synthesized on Si (100) and $Al_2O_3$ (001) substrates using a magnetron sputtering system (FJL560CI2, SKY, Shenyang, China), as shown in Figure 1. Si was used to test the crystal structure and mechanical properties; $Al_2O_3$ was used to test the friction properties. The high-purity (99%) $ZrB_2$ and Mo targets were controlled by two radio-frequency (RF) cathodes. When the base pressure of the system was less than $3 \times 10^{-4}$ Pa, the high-purity Ar gas (99.999%) at a pressure of 0.5 Pa was introduced into the chamber. $ZrB_2$/Mo multilayers were deposited by rotating the sample holder, alternately exposing the substrates to the $ZrB_2$ and Mo targets. The RF modes were 100 W and 80 W at a constant substrate bias of −40 V and a working pressure of 0.5 Pa. The modulation period of each sample was 25 nm, which corresponded to 20 cycles, after which the top layers of all samples were $ZrB_2$. By changing the sputtering time of the $ZrB_2$ and Mo targets, a series of $ZrB_2$/Mo multilayers with different modulation ratios ($t_{ZrB2}$:$t_{Mo}$ = 1:1, 2:1, 3:1, 4:1, 5:1, 6:1, 7:1, and 8:1) were obtained. Total thickness of the multilayers was around 500–600 nm.

The high-temperature tribological performance of the multilayers were measured using a high temperature tribometer (THT, Anton Paar, Austria). In the tribological experiment, the ball-on-disk structure was selected. The friction pair was an $Al_2O_3$ ceramic ball with a diameter of 6 mm. The friction radius was 4 mm, and the load was 1N. The relative sliding speed was 20 mm/s, and the friction period was 100 cycles. The test temperatures were room temperature (25 °C), 100 °C, 200 °C, 300 °C, 400 °C, and 500 °C. Sample crystallinity was analyzed by X-ray diffraction (XRD, D8A, Bruker, Germany) using a D/MAX 2500 diffractometer operated with Cu-Kα radiation at 1.54056 Å in the range of 20°–80°. The step size and dwell time of θ–2θ were 0.02 and 7.76 s, respectively. The chemical state and composition of samples were determined by X-ray photoelectron spectroscopy (XPS, PHI5000VersaProbe) with an Al-Kα source. Sample morphology was observed by scanning electron microscopy (SEM, TDCLS-8010, Hitachi, Japan) and transmission electron microscopy (TEM, JEOL JEM-3000F, Tokyo, Japan). The operation voltage of TEM was 300 KV. The hardness and elastic modulus of the multilayers were measured using a Nano Indenter system (STEP6, Anton Paar, Austria). The maximum indention depth for all samples was kept at 15% of the coating thickness to minimize the substrate effects.

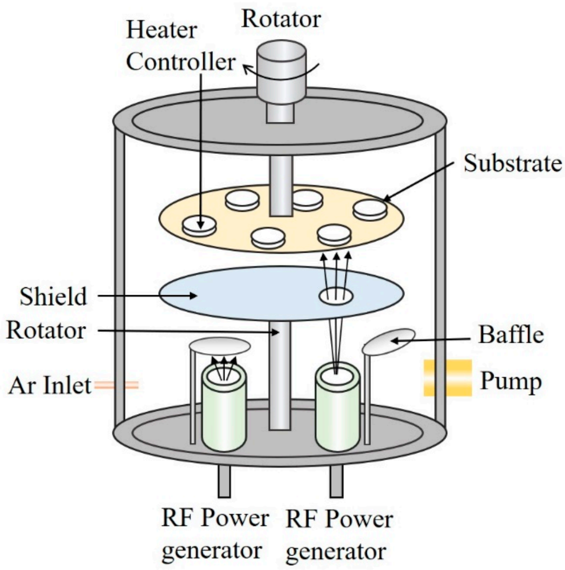


**Figure 1.** Schematic diagram of the FJL560CI2 magnetron sputtering system. RF: radio-frequency.

## 3. Results and Discussion

### 3.1. Friction Properties

Figure 2a shows the average friction coefficients of $ZrB_2$, Mo monolayers, and $ZrB_2$/Mo multilayers at different $t_{ZrB2}$:$t_{Mo}$ at different temperatures. The average friction coefficient of the $ZrB_2$ monolayer was 1.1 at room temperature, Figure 2a, which was much higher than that of the Mo monolayer (0.29). For $ZrB_2$/Mo multilayers, the average friction coefficients of $t_{ZrB2}$:$t_{Mo}$ = 2:1 and $t_{ZrB2}$:$t_{Mo}$ = 5:1 were about 0.47 and 0.77, respectively. It can be seen that the multilayer structure with the Mo layer in $ZrB_2$ can obviously improve the friction performance of $ZrB_2$, and the higher the Mo content, the better the friction performance. It can be seen from Figure 2a that with the experimental temperature increasing from 100 °C to 500 °C, the change trend of the average friction coefficient was to increase first and then decrease. The average friction coefficient of $t_{ZrB2}$:$t_{Mo}$ = 5:1 increased from 1.11 to 1.38 at 100 °C−300 °C, and then decreased to 1.23 at 500 °C.

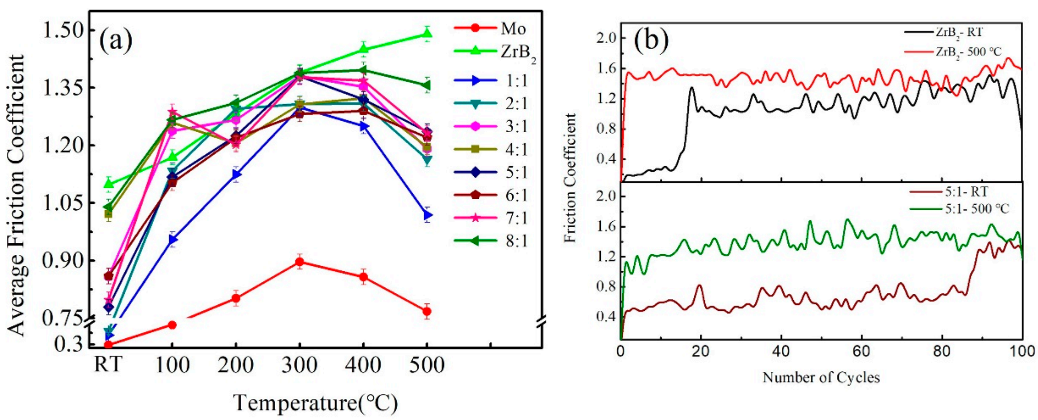


**Figure 2.** Average friction coefficients (**a**) of $ZrB_2$ and Mo monolayers and $ZrB_2$/Mo multilayers at different temperatures. The friction coefficient curves (**b**) of $ZrB_2$ and $ZrB_2$/Mo ($t_{ZrB2}$:$t_{Mo}$ = 5:1) at room temperature and 500 °C.

In contrast, the friction experiment of the $ZrB_2$ monolayer at 500 °C was 1.48, which indicates that the addition of the Mo layer can effectively improve the high-temperature friction properties of the $ZrB_2$ monolayer. This can be attributed to the oxidation reaction that occurs during the friction test. The multilayer structure is destroyed by oxides at high temperatures, resulting in changes in hardness, thereby affecting the friction and wear properties of the coating. However, these oxides play a self-lubricating role in the friction process. In a $ZrB_2$/Mo multilayers system, the oxides of zirconium or molybdenum formed on the wear surface have a low shear modulus and high self-lubricating properties, which can effectively improve the wear resistance of the multilayers [21–23]. Therefore, although the increase of temperature leads to deterioration of the friction environment and an increase of the friction coefficient, with the continuous increase of temperature, the amount of oxide increases and the friction coefficient decreases. From the friction curve of a single layer $ZrB_2$ monolayer, it can be seen that the substrate was rapidly damaged at room temperature or 500 °C, and the damage degree was more serious at 500 °C, which is consistent with the observation results of wear scar surface morphology. However, the friction curves of $t_{ZrB2}$:$t_{Mo}$ = 5:1 were obviously improved at room temperature and 500 °C. Among them, according to the friction curve of $t_{ZrB2}$:$t_{Mo}$ = 5:1 at room temperature in Figure 2b, the friction coefficient of the first 20 cycles was between 0.5–0.7, while that of 21–80 cycles was about 0.45, and that of the last 20 cycles was about 0.9. The reason may be that the oxide content in the wear marks at 25 °C is very low. In contrast, water vapor and other lubricating particles play a more important role in reducing wear marks. In the 21–80 cycles of the friction test, more self-lubricating oxide phases accumulated on the surface of the wear marks, thereby further reducing the friction coefficient. After 80 cycles, the coefficient of friction was usually attributed to film shedding and friction stability.

To understand the wear mechanism of the $ZrB_2$/Mo multilayers, a detailed study of the worn surfaces at different parameters was done under an optical microscope. Figure 3 gives the optical images of the worn surfaces of the $ZrB_2$/Mo ($t_{ZrB2}$:$t_{Mo}$ = 5:1) multilayer and $ZrB_2$ monolayer at room temperature and 500 °C. In Figure 3a,b, the wear marks of both films at room temperature were very shallow, and the wear mechanism was mainly abrasive wear. As the temperature increased, the degree of wear increased gradually. The worn surfaces of both films at 500 °C are shown in Figure 3c,d. The surfaces of both films were compact and complete. The wear marks were wide and uniform with obvious grooves. Although no obvious accumulation of wear debris was observed for the $ZrB_2$/Mo multilayer, some wear marks were deeper than the multilayer thickness and approached the hard substrate. In the area A of Figure 3d, the film obviously fell off and exposed the substrate. This is because under severe wear conditions, the multilayer was quickly worn off or even fell off, losing the wear resistance of the $ZrB_2$/Mo multilayer. The reason for the furrow is that the hardness of the $ZrB_2$/Mo multilayer decreased at 500 °C, and the convex parts of the multilayer surface cut the friction pairs and the particles with sharp corners. In contrast, the substrate deposited by the $ZrB_2$ monolayer was almost completely exposed. The color of the wear marks was also dark at room temperature, indicating a poor wear resistance. Therefore, inserting Mo into $ZrB_2$ to prepare the multilayers effectively improved the friction performance of the $ZrB_2$/Mo multilayer.

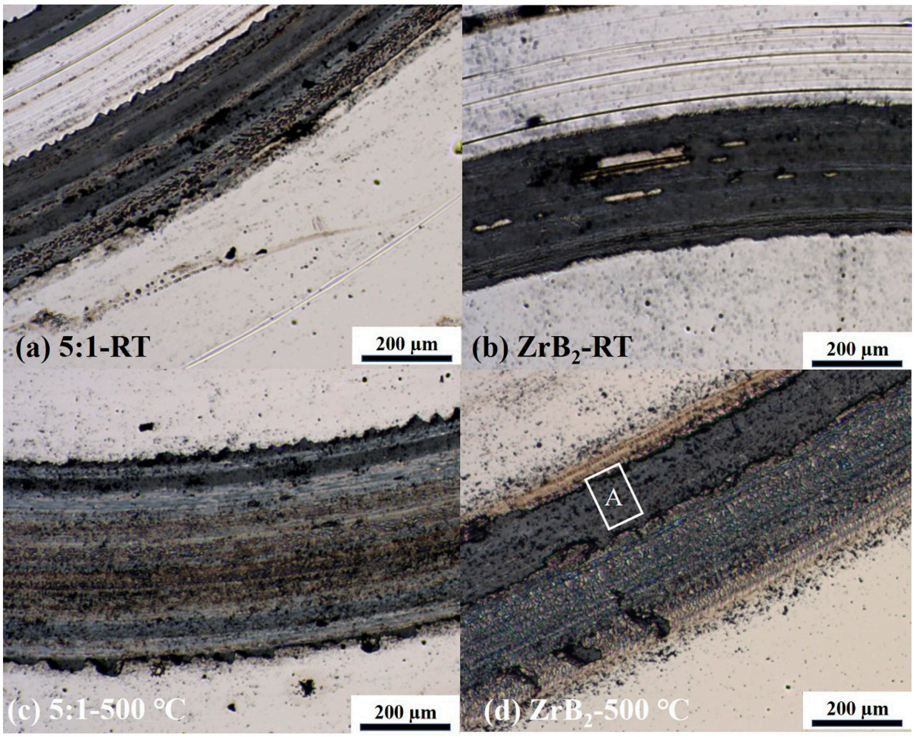


**Figure 3.** Worn surfaces topography of the $ZrB_2$/Mo ($t_{ZrB2}$: $t_{Mo}$ = 5:1) (**a**,**c**) and $ZrB_2$ (**b**,**d**) at different temperatures.

*3.2. Mechanical Properties and Microstructures*

Figure 4 shows the XRD patterns of the $ZrB_2$ and Mo monolayers along with the $ZrB_2$/Mo multilayers at different $t_{ZrB2}$:$t_{Mo}$, and the XRD partial magnification of the image. The $ZrB_2$ monolayer presented a strong (001) texture, which had a hexagonal structure, and the Mo monolayer had a (110) preferred orientation. In all multilayers, there existed a (101) preferred orientation of $ZrB_2$, but (001) disappears. This may be because the two substances grew alternately and inhibited each other, leading to the disappearance of the (001) peak. At the same time, the (110) peak of Mo could still be found in the diffraction spectrum. The single diffraction peak was caused by the tensile and compressive stresses in the epitaxial growth of Mo and $ZrB_2$ modulation layer, which made the spacing of the corresponding crystal planes close to each other [24,25]. Among the $ZrB_2$/Mo multilayers, the peak intensity was the lowest in $t_{ZrB2}$:$t_{Mo}$ = 8:1, and only weak eutectic peaks appeared. This indicates that too big a modulation ratio is not conducive to the formation of a polycrystalline structure.

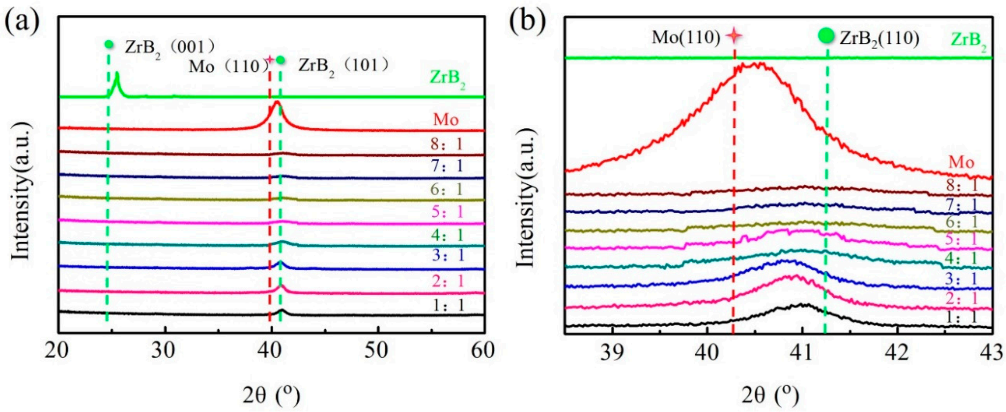


**Figure 4.** The XRD patterns of the $ZrB_2$ and Mo monolayers along with the $ZrB_2$/ Mo multilayers with different $t_{ZrB2}$:$t_{Mo}$ (**a**), and the XRD partial magnification of the image (**b**).

The periodic structure information and the composition distribution of the multilayers were obtained by XPS depth analysis. The multilayers at $t_{ZrB2}$:$t_{Mo}$ = 1:1 were sputtered along the depth for 3 min, 6 min, 9 min, 12 min, 15 min, 18 min, 21 min, 24 min, 27 min, 30 min, and 33 min, respectively. The relationship between the concentration of Zr, B, and Mo atoms and the stripping time were calculated, as shown in Figure 5a. They indicate the alternating modulation structure of $ZrB_2$ and Mo in the $ZrB_2$/Mo multilayers.

In order to prove the consistency of the periodic structure between the observed and measured values, the cross-sectional SEM image of the $ZrB_2$/Mo multilayers at $t_{ZrB2}$:$t_{Mo}$ = 1:1 is given in Figure 5b, where the dark and bright layers correspond to the Mo and $ZrB_2$ layers, respectively. The interfaces of $ZrB_2$ and Mo are clear, proving the formation of an obvious modulation structure, which is consistent with the depth analysis of XPS.

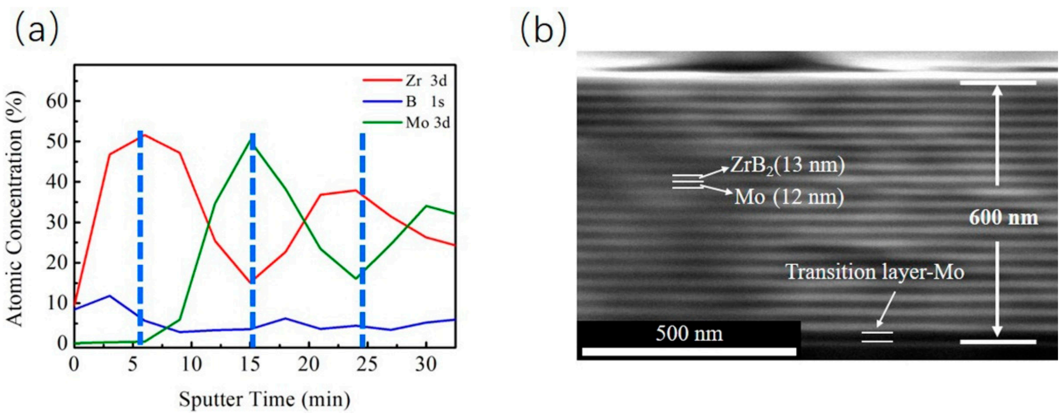


**Figure 5.** The relationship between the atomic concentration and the stripping time (**a**) and the cross-sectional SEM image (**b**) of the $ZrB_2$/Mo multilayers with $t_{ZrB2}$:$t_{Mo}$ = 1:1.

The structure characteristics of the $ZrB_2$/Mo multilayers can be further reflected by the cross-sectional HRTEM images. As shown in Figure 6, interface diffusion of the $ZrB_2$/Mo multilayer $t_{ZrB2}$:$t_{Mo}$ = 4:1 occurs, and part of the atom-mixing region appears at the interface, which is a benefit for the improvement of mechanical properties. The diffraction ring in the SAED pattern shows the Mo (110) crystal phase and the $ZrB_2$ (001) crystal phase. These results are in agreement with the qualitative analysis provided by XRD. The presence of small grains and amorphous phases would hinder the interface layer and fault slip, and make each sub-layer more compact. This structure plays a positive role in improving the mechanical properties of the $ZrB_2$/Mo multilayers. Meanwhile, the tribological performance was improved.

In order to further analyze the surface elements and the bonding state of the $ZrB_2$/Mo multilayers, the surface of the multilayer at $t_{ZrB2}$:$t_{Mo}$ = 1:1 was scanned by XPS. It can be seen from Figure 7a that the main components on the surface were Zr, B, and Mo elements. The appearance of the O element is related to an amount of oxygen left in the equipment cavity. According to the Mo3*d* spectra shown in Figure 7b, the two main peaks at 227.8 eV (3*d*5/2) and 230.9 eV (3*d*5/2) are related to metallic Mo, and the positions of these two peaks are separated by about 3.1 eV [26]. In addition, there are two secondary peaks located at 231 eV (3*d*3/2) and 228 eV (3*d*5/2), respectively. Figure 7c exhibits the narrow spectrum of Zr3*d*, which splits into two strong peaks, Zr3*d*5/2 and Zr3*d*3/2, and the positions of these two peaks are separated by about 2.3 eV. The Zr3*d*5/2 could be assigned to two sub-peaks: $ZrB_2$ (178.6 eV) and $ZrO_2$ (183.3 eV); whereas the Zr3*d*3/2 is composed of another three sub-peaks: $ZrB_2$ (180.9 eV), $O_2$/Zr (185.8 eV), and $ZrO_2$ (186.6 eV) [27,28]. Meanwhile, the width and intensity of the 3*d*5/2 and 3*d*3/2 sub peaks of $ZrB_2$ are much higher than that of $ZrO_2$ in Figure 7c. Therefore, Zr and B atoms mainly exist in the state of the Zr-B bond in the multilayers.

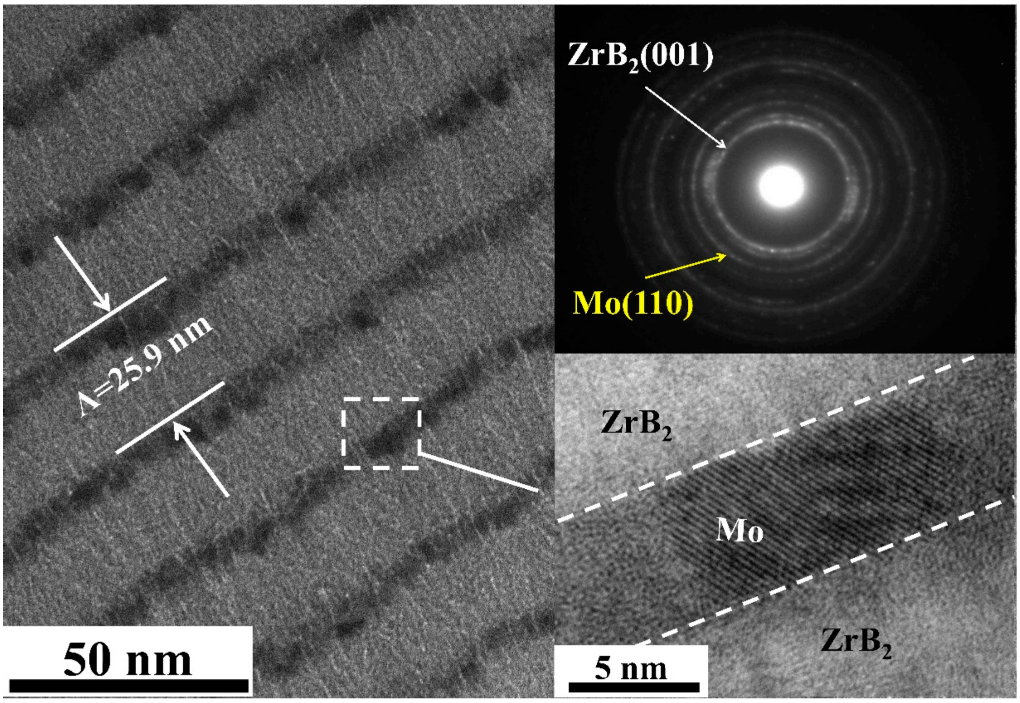


**Figure 6.** Cross-sectional HRTEM images of the $ZrB_2$/Mo multilayer at the modulation ratio of 4:1.

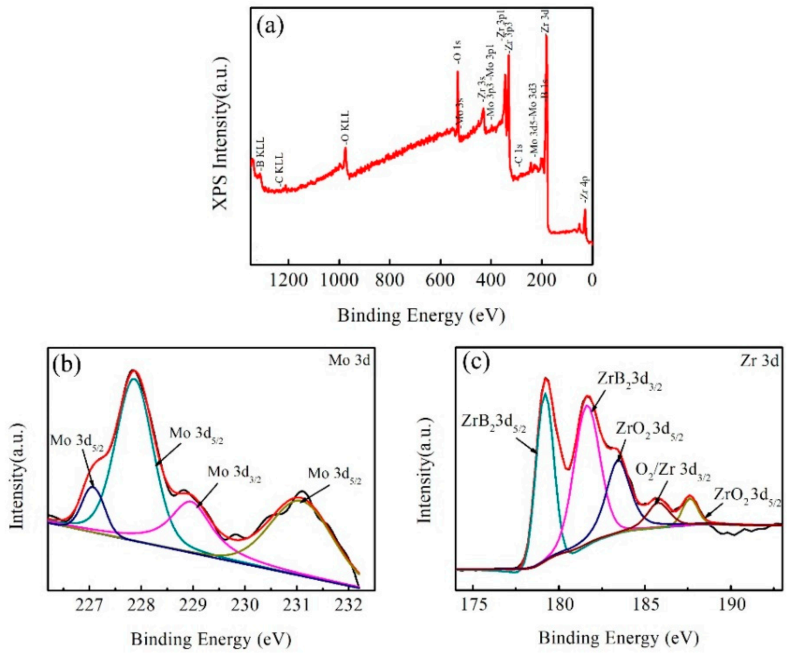


**Figure 7.** High resolution XPS spectra of (**a**) valence band spectra of surface elements, (**b**) Mo3*d*, and (**c**) Zr3*d* of the $ZrB_2$/Mo multilayers with modulation ratio of $t_{ZrB2}$:$t_{Mo}$ = 1:1.

Figure 8a,c shows the hardness, elastic modulus, and coefficient of $ZrB_2$ and Mo monolayers and $ZrB_2$/Mo multilayers at different $t_{ZrB2}$:$t_{Mo}$ at room temperature. Changes in the $t_{ZrB2}$:$t_{Mo}$ gradually increased the elastic modulus and hardness increased and then decreased, but the hardness of the multilayer was mostly higher than the hardness of the monolayer. The change trend of the elastic modulus was similar to that of hardness. The trend of the friction coefficient increased with the change of $t_{ZrB2}$:$t_{Mo}$, then decreased, and then increased again. Figure 8b,d shows the hardness and friction coefficient of the $ZrB_2$ monolayer and $ZrB_2$/Mo multilayers at $t_{ZrB2}$:$t_{Mo}$ = 5:1 at different temperatures. The $t_{ZrB2}$:$t_{Mo}$ of 5:1 corresponds to the maximum hardness (26.1 GPa) and the maximum elastic modulus (241.99 GPa) of $ZrB_2$/Mo multilayer at room temperature, and the corresponding friction coefficient was 0.77. Its hardness at 500 °C was 8.9 GPa, and the corresponding friction coefficient was 1.23. Compared with the $ZrB_2$ monolayers, the hardness and friction coefficient of the multilayer was significantly improved at different temperatures.

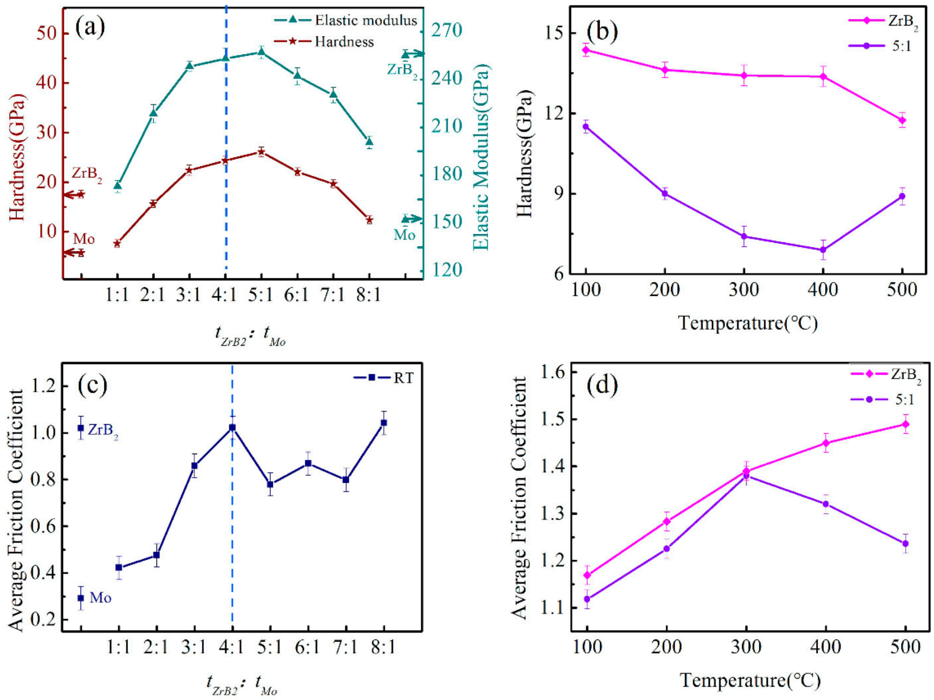


**Figure 8.** The hardness, elastic modulus (**a**) and friction coefficient (**c**) of $ZrB_2$/Mo multilayers with different modulation ratios at room temperature, as well as the hardness (**b**) and friction coefficient (**d**) of $ZrB_2$ and $ZrB_2$/Mo ($t_{ZrB2}$:$t_{Mo}$ = 5:1) at different temperatures.

The $t_{ZrB2}$:$t_{Mo}$ was in the range of 1:1~4:1, the influence of the friction coefficient was not directly related to the change of hardness. According to the TEM results, it is speculated that $ZrB_2$ is not crystallized at this stage. The Mo layer and $ZrB_2$ layer were not affected during the growth process. The change of hardness conformed to the mixed hardness rule and it was the result of components hardening, so the hardness increased while the friction performance was not improved. Combined with the results of XPS, during the preparation process, oxygen easily entered into $ZrB_2$ to form $ZrO_2$ with larger volume, which further led to the increase of surface roughness and the friction coefficient.

In contrast, when the $t_{ZrB2}$:$t_{Mo}$ was in the range of 4:1 to 8:1, hardness and friction coefficient showed an approximate opposite trend. This seems to reveal a certain connection between hardness and the friction coefficient, which indicates that the higher the hardness, the lower the friction coefficient, and vice versa. Zhang and Li confirmed this [29,30]. In combination with TEM results, the crystal phase (001) appeared in $ZrB_2$. The same situation occurred in the heating conditions. The hardness of the films decreased significantly with the increase of temperature, and an obvious turning point in the friction coefficient appeared at 300 °C, which may be caused by the release of residual stress due to temperature [31]. However, the modulation structure remained stable.

It seems difficult to explain the above phenomenon with a unified law like Hall-petch reinforced materials [32], coherent epitaxial theory [33], interface stress effect [34], or dislocation slip hindered by the interface [35]. Since these theories are difficult to apply to the situation under high temperature, the changes in hardness and the friction coefficient under high temperature can be explained by the oxidation caused by temperature increase [36]. However, energy spectrum results have shown that the oxidation process hardly affects the inside of the multilayers. Therefore, in order to understand the nature of hardness's influence on the friction coefficient, a theoretical explanation at the atomic level is necessary.

### *3.3. Mechanism of Friction Behavior*

From the above experimental results, the friction coefficient of the $ZrB_2$/Mo multilayers system under the synergism of effective modulation ratio and temperature can be seen. It always seems to be positively correlated with the hardness to a certain extent, that is, the lower the hardness, the higher the friction coefficient, which is consistent with the results of most literature [37–39]. However, most researchers fail to reveal this essence. For the $ZrB_2$-Mo interface, $ZrB_2$ is prone to galling, whereas Mo is slightly more resistant to galling. Since the bonding characteristics and adhesive properties may play a vital role in the material transfer, i.e., galling, it is of great interest to evaluate the bonding characteristics and strength between the two sliding metals [40]. Based on previous research work, Jin used the first-principles method to study the structure of the TaN (100)/$ReB_2$ (001) interface and showed that the stability of the interface is closely related to the interface viscous work [41]. Combined with previous research methods, the first principles are employed in the current work to explain the influence of the interface structure on the friction coefficient by establishing an interface structure model, combining state density, atomic structure, interface energy, ideal adhesion work, and charge distribution.

In the first principle calculation, the four models (Figure 9) of the $ZrB_2$ (001)/Mo (110) interface are established according to the XRD results, and the interface properties of the model are effectively analyzed by the density functional theory (in order to ensure that the interface of the two parts fully represented the performance of the bulk material, through the surface energy convergence test, we selected, for both $ZrB_2$ and Mo, an atomic layer thickness of 9 layers, a cutoff energy of 450 eV, K point was $6 \times 6 \times 6$, and the energy error was within 1–2 MeV/atom). In addition, the interface energy ($\gamma$int) and ideal cohesion energy ($W_{ad}$) can be used to evaluate the bonding strength and stability of the interface [42]. So, we calculate the four models of ideal interface viscous work and the interface spacing (as shown in Table 1). It can be seen that the ideal viscous work of the interface with B as the terminal is generally greater than that with Zr as the terminal, and the interface energy is generally less than that with Zr as the terminal. Model 2 has the largest interfacial viscous work, the smallest interfacial energy, and the smallest interface spacing.

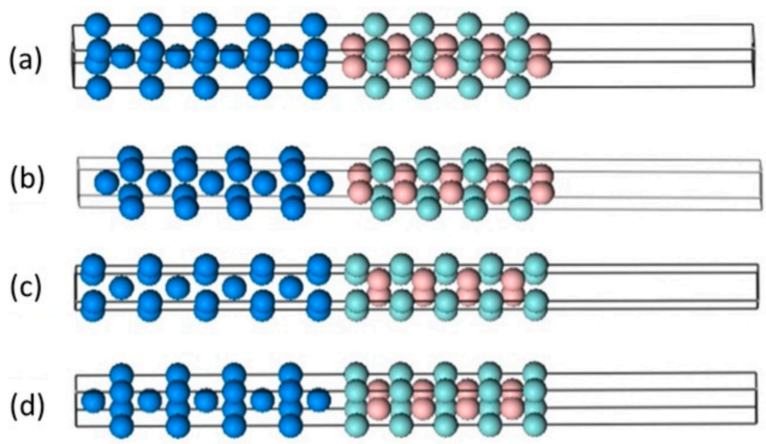


**Figure 9.** Four interface models of $ZrB_2$/Mo: model 1 (**a**), model 2 (**b**) taking B as the terminal, model 3 (**c**) and model 4 (**d**) taking Zr as the terminal.

**Table 1.** The interface distance of the four interface models of the $ZrB_2$/Mo multilayers, the ideal interface viscosity work, and the interface energy.

| Stacking | | d (Å) | $W_{ad}$ (J/m$^2$) | $\gamma$ (eV/Å$^2$) |
|---|---|---|---|---|
| B-terminated | Model 1 | 2.958 | 6.227 | −0.1690 |
| | Model 2 | 1.070 | 6.233 | −0.1693 |
| Zr-terminated | Model 3 | 3.000 | 2.778 | 0.0463 |
| | Model 4 | 3.000 | 4.755 | −1.2351 |

In order to further investigate the bonding mechanism of the $ZrB_2$ (001) and Mo (110) interface, the partial density of the state of the stable interface (Model 2) was calculated (where the first layer is closer to the interface and the ninth layer is farther from the interface), as shown in Figure 10. The states at $E_F$ of each layer have significant peaks, indicating that $ZrB_2$, Mo block, and the interface have metallic properties, while the other states are close to zero, indicating semiconductor properties. It is obvious that Mo (Zr) *d* and B*p* states are hybridized at $E_F$, which indicates that Mo (Zr) and B with strong orbital hybridization and strong covalent bonds are formed. In addition, the partial density of states (PDOS) of Mo and B atoms are very similar to that of their bulk atoms, which means that the interface transition from $ZrB_2$ to Mo is smooth except for the atomic structure. It was also found that the peak of atoms in the interface layer is obviously different from that of the bulk materials, while the peaks of atoms far away from the interface layer are similar to those of the bulk materials. Although the overall PDOS characteristics of the 9th layer are slightly different from those of the bulk materials, it can still be seen that the surface effect only affects one or two atomic layers [43].

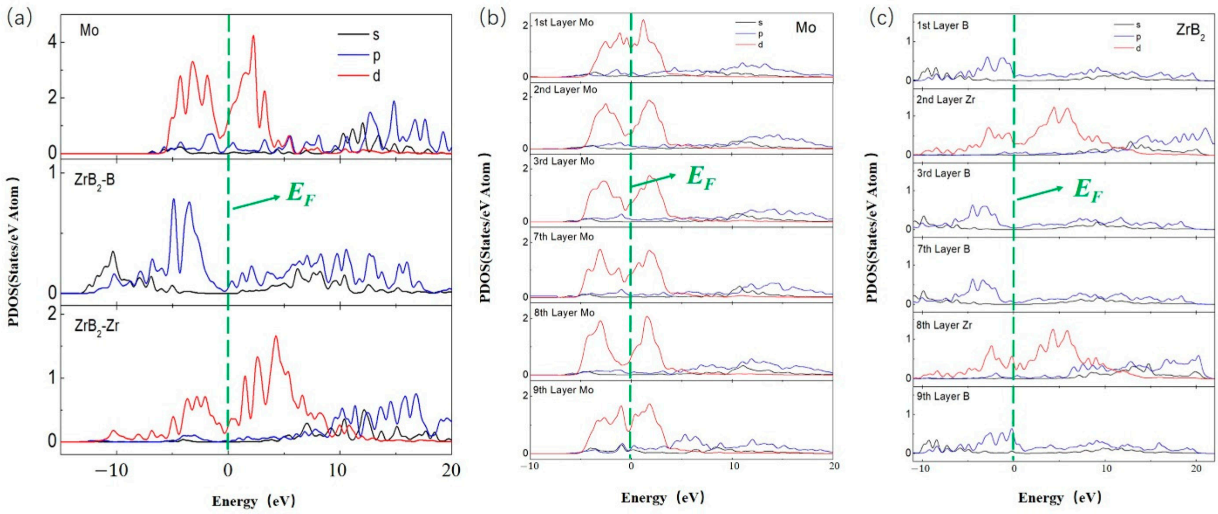


**Figure 10.** DOS (density of state) projected on the most stable interface after relaxation. (**a**) The partial density of states (PDOS) for bulk Mo and $ZrB_2$; (**b**) the PDOS of the Mo layers; and (**c**) the PDOS of the $ZrB_2$ layers. The $E_F$ is set to zero, denoted by a dash line.

Although PDOS can reveal the information of covalent bonding, we still need to choose the information of ionicity and electron transfer, which can be obtained from the charge-density and charge-density difference of the (110) surface of Mo, Zr, and B atoms at the interface, as shown in Figure 11. In the charge density (Figure 11a) of the $ZrB_2$/Mo interface (Model 2), it can be found that significant charge accumulation occurs between interfacial B and Mo atoms in the $ZrB_2$/Mo interfaces, indicating that extremely strong covalent bonds are formed in the interface. Usually, the covalent bonds can cause stronger interactions. Moreover, after full relaxation, the small distance between interfacial B and Mo atoms enhances their strong interaction. In the charge density differences (Figure 11b) of the $ZrB_2$/Mo interface (Model 2), it shows that due to the interaction of interface layer atoms, Mo-Mo is obviously stretched out for a certain distance. Therefore, a part of the Mo-Mo region is close to the B direction, and then part of the charges of the Mo atoms at the interface are transferred to the interface B atoms to form the ionic bonds, that is, the strong interaction between B and Mo [42,44]. In addition, from the perspective of charge accumulation, the charges are mainly concentrated near the B layer. The accumulation of charges is a typical feature of polar covalent bonds. The more charge that accumulates, the stronger the covalent property and the stronger the interface bond [44]. This provides a strong support for Model 2 to have more ideal viscous work, and also explains that Model 2 is the most stable structure among the four interface models [43].

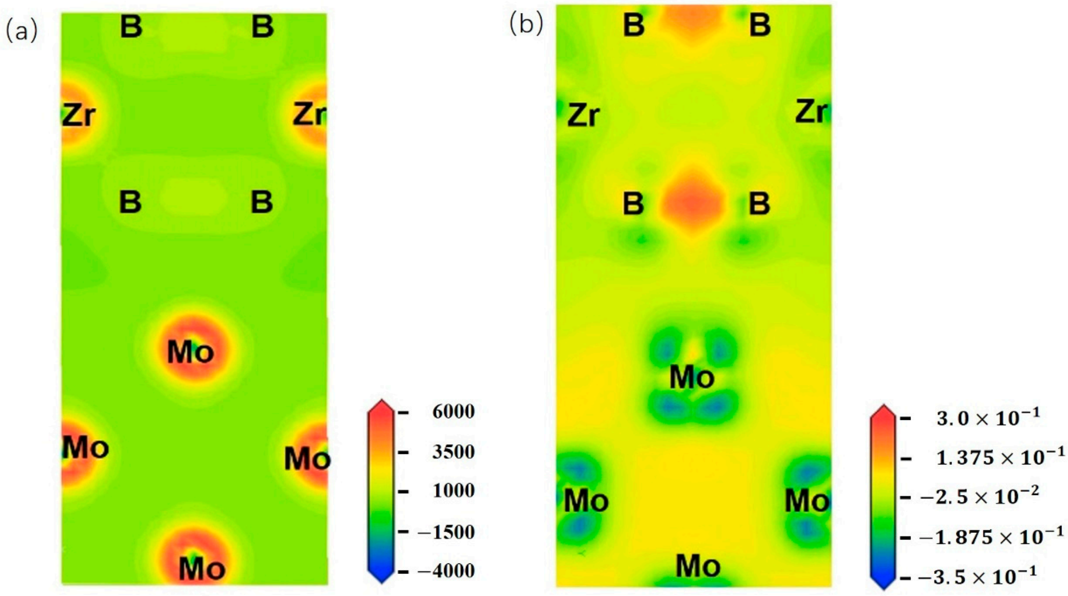


**Figure 11.** Distribution of (**a**) charge density and (**b**) charge density difference along the (110) direction for the $ZrB_2$/Mo interface in Model 2.

The existence of covalent bonds and ionic bonds makes the interface have more viscous work, and the interface bonding is more stable, thus improving the hardness of the $ZrB_2$/Mo multilayer system. The increase of hardness also improves the wear resistance. Therefore, the new bonding changes the bonding mode and strength between atoms at the interface, and then affect the mutual transfer of charges. It can further prevent the sliding between atomic layers, and improve the bonding strength, toughness, and macroscopic properties of the interface. In conclusion, the growth mechanism of $ZrB_2$/Mo multilayers is the root cause of the improvement of their mechanical and friction properties, and the atomic structure between the interfaces can indeed affect the mechanical and friction properties of materials from a microscopic perspective.

## 4. Conclusions

$ZrB_2$/Mo multilayers were synthesized on Si (100) and $Al_2O_3$ (001) substrates by magnetron sputtering. The effects of structure on the mechanical and friction behavior of $ZrB_2$/Mo multilayers were investigated. In the $ZrB_2$/Mo multilayer system ($t_{ZrB2}$:$t_{Mo}$ = 5:1), the maximum hardness at room temperature was 26.1 GPa and the friction coefficient was 0.86. At 500 °C, the results show that the effective modulation was formed when $ZrB_2$ (001) and Mo (110) phases appeared simultaneously. The friction coefficient decreased with the increase of hardness under the synergy of temperature and an effective modulation ratio, showing an approximately opposite change rule. The results of calculations based on the first principles proved that when the effective modulation structure was not affected by temperature, that is, when the interface between $ZrB_2$ (001) and Mo (110) was stable, the stability of the interface determined the hardness and friction coefficient of the $ZrB_2$/Mo multilayers. Through the experimental research, it was found that this method was a simple and effective way to modulate the friction coefficient of the multilayers.

**Author Contributions:** Conceptualization, D.L.; data curation, T.Z.; formal analysis, L.D.; investigation, T.Z., L.D., and J.W.; methodology, T.Z., L.D., and D.L.; project administration, T.Z. and D.L.; resources, J.W.; writing—original draft preparation, T.Z.; writing—review and editing, L.D., J.W., and D.L. All authors have read and agree to the published version of the manuscript.

**Funding:** This research was funded by the Program for Innovative Research in the University of Tianjin (No. TD13-5077) and the National Natural Science Foundation of China (No. 51901158). This work was also supported by the Science & Technology Development Fund of the Tianjin Education Commission for Higher Education (No. 2018KJ158).

**Conflicts of Interest:** The authors declare no conflict of interest.

## References

1. Kumar, N.; Gautam, G.; Gautam, R.K.; Mohan, A.; Mohan, S. Wear, friction and profilometer studies of insitu AA5052/ZrB2 composites. *Tribol. Int.* **2016**, *97*, 313–326. [CrossRef]
2. Madhavan, R.; Bellon, P.; Averback, R.S. Wear Resistance of Cu/Ag Multilayers: A Microscopic Study. *ACS Appl. Mater. Interfaces* **2018**, *10*, 15288–15297.
3. Gérard, B. Application of thermal spraying in the automobile industry. *Surf. Coat. Technol.* **2006**, *201*, 2028–2031.
4. Guo, C.; Chen, J.M.; Yao, R.G.; Zhou, J.S. Microstructure and High Temperature Wear Resistance of Laser Cladding NiCoCrAlY/$ZrB_2$ Coating. *Rare Metal Mater. Eng.* **2013**, *42*, 1547–1551.
5. Yu, L.D.; Shuy, G.W.; Vilaithong, T. Friction modification of WC-Co by ion implantation. *Surf. Coat. Technol.* **2000**, *128*, 404–409. [CrossRef]
6. Walck, S.D.; Donley, M.S.; Zabinski, J.S.; Dyhouse, V.J. Characterization of pulsed laser deposited PbO/$MoS_2$ by transmission electron microscopy. *J. Mater. Res.* **1994**, *9*, 236–245. [CrossRef]
7. Walck, S.D.; Zabinski, J.S.; McDevitt, N.T.; Bultman, J.E. Characterization of air-annealed, pulsed laser deposited ZnO-$WS_2$ solid film lubricants by transmission electron microscopy. *Thin Solid Films* **1997**, *305*, 130–143. [CrossRef]
8. Aouadi, S.M.; Paudel, Y.; Luster, B.; Stadler, S.; Kohli, P.; Muratore, C.; Hager, C.; Voevodin, A.A. Adaptive $Mo_2N$/$MoS_2$/Ag tribological nanocom-posite coatings for aerospace applications. *Tribol. Lett.* **2008**, *29*, 95–103. [CrossRef]
9. Aouadi, S.M.; Paudel, Y.; Simonson, W.J.; Ge, Q.; Kohli, P.; Muratore, C.; Voevodin, A.A. Tribological investigation of adaptive $Mo_2N$/$MoS_2$/Ag coatings with high sulfur content. *Surf. Coat. Technol.* **2009**, *203*, 1304–1309. [CrossRef]
10. Sun, W.; Liu, J.; Xiang, H.; Zhou, Y. A Theoretical Investigation on the Anisotropic Surface Stability and Oxygen Adsorption Behavior of $ZrB_2$. *J. Am. Ceram. Soc.* **2016**, *99*, 4113–4120. [CrossRef]
11. Wang, P.; Qi, Y.; Zhou, S.; Hu, P.; Chen, G.; Zhang, X.; Han, W. Polycrystalline $ZrB_2$ coating prepared on graphite by chemical vapor deposition. *Phys. Status Solidi (b)* **2016**, *253*, 1590–1595. [CrossRef]
12. Ma, H.-B.; Zhang, G.-J.; Liu, H.-L.; Liu, J.-X.; Lu, Y.; Xu, F.F. Effect of WC or ZrC addition on thermal residual stresses in $ZrB_2$SiC ceramics. *Mater. Des.* **2016**, *110*, 340–345. [CrossRef]
13. Sha, J.; Li, J.; Wang, S.; Wang, Y.; Zhang, Z.; Dai, J. Toughening effect of short carbon fibers in the $ZrB_2$–$ZrSi_2$ ceramic composites. *Mater. Des.* **2015**, *75*, 160–165. [CrossRef]
14. Balak, Z.; Asl, M.S.; Azizieh, M.; Kafashan, H.; Hayati, R. Effect of different additives and open porosity on fracture toughness of $ZrB_2$-SiC-based composites prepared by SPS. *Ceram. Int.* **2017**, *43*, 2209–2220. [CrossRef]
15. Zhou, C.; Wang, P.; Wei, C.; Han, W.; Zhang, X.; Xu, B. $ZrB_2$ grains synthesized on graphite by chemical vapor deposition. *J. Alloys Compd.* **2017**, *698*, 27–32. [CrossRef]
16. Emami, S.M.; Salahi, E.; Zakeri, M.; Tayebifard, S.A. Effect of composition on spark plasma sintering of $ZrB_2$-SiC-ZrC nanocomposite synthesized by MASPSyn. *Ceram. Int.* **2017**, *43*, 111–115. [CrossRef]
17. Zhou, S.B.; Wang, Z.; Zhang, W. Effect of graphite flake orientation on microstructure and mechanical properties of $ZrB_2$-SiC-graphite composite. *J. Alloys Compd.* **2009**, *485*, 181–185. [CrossRef]
18. Silvestroni, L.; Sciti, D.; Hilmas, G.E.; Fahrenholtz, W.G.; Watts, J. Effect of a weak fiber interface coating in $ZrB_2$ reinforced with long SiC fibers. *Mater. Des.* **2015**, *88*, 610–618. [CrossRef]
19. Sciti, D.; Pienti, L.; Murri, A.N.; Landi, E.; Medri, V.; Zoli, L. From random chopped to oriented continuous SiC fibers-$ZrB_2$ composites. *Mater. Des.* **2014**, *63*, 464–470. [CrossRef]
20. Monteverde, F.; Guicciardi, S.; Bellosi, A. Advances in microstructure and mechanical properties of zirconium diboride based ceramics. *Mater. Sci. Eng. A* **2003**, *346*, 310–319. [CrossRef]
21. Xu, J.; Ju, H.; Yu, L. Effects of Mo Content on the Microstructure and Friction and Wear Properties of Timon Films. *Acta Met. Sin.* **2012**, *48*, 1132–1138. [CrossRef]
22. Hazar, H. Characterization of MoN coatings for pistons in a diesel engine. *Mater. Des.* **2010**, *31*, 624–627. [CrossRef]

23. Yang, Q.; Zhao, L.; Patnaik, P.; Zeng, X. Wear resistant TiMoN coatings deposited by magnetron sputtering. *Wear* **2006**, *261*, 119–125. [CrossRef]
24. Mei, F.; Shao, N.; Wei, L.; Dong, Y.; Li, G. Coherent epitaxial growth and superhardness effects of fcc-TiN/hcp-$TiB_2$ nanomultilayers. *Appl. Phys. Lett.* **2005**, *87*, 011906. [CrossRef]
25. Kong, M.; Shao, N.; Dong, Y.; Yue, J.; Li, G. Growth, microstructure and mechanical properties of (Ti, Al)N/VN nanomultilayers. *Mater. Lett.* **2006**, *60*, 874–877. [CrossRef]
26. Liu, C.H.; Du, X.S.; Wang, D.Z.; Huang, N.K.; Yang, B. XPS characterization of the molybdenum before and after $H^+$ ion irradiation. *J. Funct. Mater.* **2007**, *2*, 176–178.
27. Wang, T.-G.; Liu, Y.; Zhang, T.; Kim, D.-I.; Kim, K.H. Influence of Nitrogen Flow Ratio on the Microstructure, Composition, and Mechanical Properties of DC Magnetron Sputtered Zr–B–O–N Films. *J. Mater. Sci. Technol.* **2012**, *28*, 981–991. [CrossRef]
28. Pierson, J.; Billard, A.; Belmonte, T.; Michel, H.; Frantz, C. Influence of oxygen flow rate on the structural and mechanical properties of reactively magnetron sputter-deposited Zr–B–O coatings. *Thin Solid Films* **1999**, *347*, 78–84. [CrossRef]
29. Zhang, J.; Xue, Q.; Li, S.-X.; Qin, Z. Microstructure, corrosion and tribological properties of Ti(CN) multilayer coatings on 35CrMo steel by CVD. *Rare Met.* **2014**, *39*, 1314–1320. [CrossRef]
30. Li, Y.; Zou, W.J.; Li, B.X.; Dong, Q.M. The Frictional Properties and Mechanism of Nano-Diamond/Ni Composite Coatings by Brush-Plating. *Adv. Mater. Res.* **2011**, *291–294*, 197–200. [CrossRef]
31. Wang, X.; Xu, J.; Ma, S.; Xu, K. Effects of annealing temperature on the microstructure and hardness of TiAlSiN hard coatings. *Chin. Sci. Bull.* **2011**, *56*, 1727–1731. [CrossRef]
32. Anderson, P.; Li, C. Hall-Petch relations for multilayered materials. *Nanostruct. Mater.* **1995**, *5*, 349–362. [CrossRef]
33. Du, H.J.; Tian, Y.J. Hardening mechanism for Nano-multilayer films. *Acta Inorg. Mater.* **2006**, *4*, 769–775.
34. Kato, M.; Mori, T.; Schwartz, L. Hardening by spinodal modulated structure. *Acta Met.* **1980**, *28*, 285–289. [CrossRef]
35. Shinn, M.; Barnett, S.A. Effect of superlattice layer elastic moduli on hardness. *Appl. Phys. Lett.* **1994**, *64*, 61–63. [CrossRef]
36. Bouaouina, B.; Besnard, A.; Abaidia, S.; Haid, F. Residual stress, mechanical and microstructure properties of multilayer $Mo_2$ N/CrN coating produced by R.F Magnetron discharge. *Appl. Surf. Sci.* **2017**, *395*, 117–121. [CrossRef]
37. Drnovsek, A.; de Figueiredo, M.R.; Vo, H.; Xia, A.; Vachhani, S.J.; Kolozsvari, S.; Hosemann, P.; Franz, R. Correlating high temperature mechanical and tribological properties of CrAlN and CrAlSiN hard coatings. *Surf. Coat. Technol.* **2019**, *372*, 361–368. [CrossRef]
38. Kiryukhantsev-Korneev, F.V.; Lemesheva, M.V.; Shvyndina, N.V.; Levashov, E.A.; Potanin, A.Y. Structure, Mechanical Properties, and Oxidation Resistance of $ZrB_2$, ZrSiB, and ZrSiB/SiBC Coatings. *Prot. Met. Phys. Chem. Surf.* **2018**, *54*, 1147–1156. [CrossRef]
39. Lu, Z.-L.; Zhou, Y.-X.; Rao, Q.-C.; Jin, Z.-H. An investigation of the abrasive wear behavior of ductile cast iron. *J. Mater. Process. Technol.* **2001**, *116*, 176–181. [CrossRef]
40. Tarasov, S.; Rubtsov, V.; Kolubaev, E.; Gnyusov, S.F.; Kudinov, Y.A. Radioscopy of remnant joint line in a friction stir welded seam. *Russ. J. Nondestruct. Test.* **2015**, *51*, 573–579. [CrossRef]
41. Jin, S.X.; Liu, N.; Zhang, S.; Li, D.J. The simulation of interface structure, energy and electronic properties of TaN/$ReB_2$ multilayers using first-principles. *Surf. Coat. Technol.* **2017**, *326*, 417–423. [CrossRef]
42. Xiong, H.; Liu, Z.; Zhang, H.; Du, Z.; Chen, C. First principles calculation of interfacial stability, energy and electronic properties of SiC/$ZrB_2$ interface. *J. Phys. Chem. Solids* **2017**, *107*, 162–169. [CrossRef]
43. Fan, X.; Chen, B.; Zhang, M.; Li, D.; Liu, Z.; Xiao, C. First-principles calculations on bonding characteristic and electronic property of TiC (111)/TiN (111) interface. *Mater. Des.* **2016**, *112*, 282–289. [CrossRef]
44. Wang, H.; Zhang, S.; Li, D.; Liu, S. The simulation of adhesion, stability, electronic structure of W/$ZrB_2$ interface using first-principles. *Surf. Coat. Technol.* **2013**, *228*, S583–S587. [CrossRef]